Article

Baseline temperature variability shapes the geographical distribution of future hot extremes under anthropogenic warming

Check for updates

Zhili Tang[1,2], Shenghui Zhou[3], Xiaohui Ma [1,3] ✉, Lixin Wu [1,3], Wenju Cai [1,3,4,5], Zhao Jing [1,3], Zhaohui Chen [1,3] & Bolan Gan [1,3]

The intensifying hot extreme events under anthropogenic warming severely affect human health and the natural environment, yet the factors driving their heterogeneous geographical distribution remain unclear. Here we utilize an eddy-resolving high-resolution climate model alongside multiple simulations from Coupled Model Intercomparison Project Phase 6, we find baseline temperature variability as a key factor shaping the global distribution of projected hot extremes, with over 80% of the global increase in hot extremes anticorrelated with baseline temperature variability, a relationship interpretable within the signal-to-noise ratio framework. We further demonstrate that the baseline temperature variability is anchored by persistent land-atmosphere coupling, which endures over century timescales and sustains the spatial heterogeneity of future hot extremes. Our findings suggest that baseline temperature variability could serve as a potential indicator for future hot extreme distribution, offering valuable insights for developing targeted adaptation strategies and improving regional resilience.

Hot extreme events, characterized by prolonged periods of excessively high temperatures exceeding the average, have devastating impacts on human health, agriculture, and the natural environment[1–4]. One of the most severe events, the 2003 European heatwave, led to approximately 70,000 deaths and more than €15 billion in economic loss[5,6]. Similarly, the 2010 Russian heatwave resulted in over 55,000 deaths and a 25% reduction in crop production[7]. Under climate change, these events are expected to increase in frequency, intensity, and duration[8]. Importantly, the geographical response of hot extremes to anthropogenic warming is highly heterogeneous, with some regions experiencing far more intense extremes than the global average, leading to disproportionately socioeconomic impacts[9–11]. Understanding the mechanisms behind the spatial heterogeneity is essential for systematically improving regional climate projections for adaptation strategies.

While there is broad consensus regarding the increasing occurrence, magnitude of hot extremes under anthropogenic warming[12–15], far less attention has been devoted to their spatial heterogeneity and the underlying drivers remain unclear. Researchers have approached the problem from an idealized statistical perspective, highlighting changes in the thermal distribution, particularly shifts in the mean, variability, and skewness of temperature[16–18]. Although the influence of rising mean temperature on extremes is well established, the contribution of variability remains debated. Emerging studies identify the role of baseline variability in shaping the regional disparities of future extremes[19–21], yet this impact is sensitive to the definition and threshold of extremes and can even yield opposite effects[22,23].

Identifying the physical processes underlying these statistical relationships and unraveling how they drive the geographical distribution of projected hot extremes remains particularly challenging. One widely discussed driver is a soil moisture-temperature feedback, where decreasing soil moisture leads to rising mean temperature due to reduced evaporation, and vice versa[10,24,25]. The feedback plays a crucial role in amplifying regional hot extremes, particularly in midlatitude regions. In high-latitude regions, snow/ice-temperature feedback modifies surface albedo, further affecting warming[26]. Additionally, atmospheric dynamical processes, such as blocking events and large-scale circulation patterns, contribute to the regional variability of hot extremes. For example, intense European heatwaves have been linked to weakened atmospheric circulation and increased atmospheric blocking[27–29]. Sea surface temperatures may also impact adjacent

[1]Frontiers Science Center for Deep Ocean Multispheres and Earth System and Key Laboratory of Physical Oceanography, Ocean University of China, Qingdao, China. [2]Frontiers Science Center for Deep Ocean Multispheres and Earth System and Key Laboratory of Physical Oceanography/Academy of Future Ocean, Ocean University of China, Qingdao, China. [3]Laoshan Laboratory, Qingdao, China. [4]State Key Laboratory of Loess and Quaternary Geology, Institute of Earth Environment, Chinese Academy of Sciences, Xi'an, China. [5]State Key Laboratory of Marine Environmental Science & College of Ocean and Earth Sciences, Xiamen University, Xiamen, China. ✉e-mail: maxiaohui@ouc.edu.cn

land hot extremes by altering atmospheric circulation and heat advection[30–32]. These drivers are intricately connected—soil moisture can modulate atmospheric circulation, exacerbating hot extremes[33]; while changes in atmospheric circulation can feedback onto soil moisture and sea surface temperature[34], creating a complex interaction system. Moreover, large uncertainties in the future evolution of soil moisture, snow/ice and atmospheric circulation in current climate models[8,35–37] add difficulty to accurately projecting how hot extremes will manifest regionally under anthropogenic warming.

The issue of whether there is a systematic predictive indicator for the projection of regional variability in future hot extremes is critical yet unresolved. In this study, we analyze outputs from a set of eddy-resolving, high-resolution simulations from Community Earth System Model (HR-CESM) with ~0.25° atmospheric and ~0.1° oceanic resolution and 10 climate models in Coupled Model Intercomparison Project Phase 6 (CMIP6, see High-Resolution CESM and CMIP6 simulations in Methods; Supplementary Table 1), to investigate the statistical factors and associated physical processes driving the spatial heterogeneity of future hot extremes in warming climate.

Results

Simulated and projected hot extremes in HR-CESM and CMIP6

We first evaluate the models' ability to simulate the observed characteristics of hot extreme events, including occurrence frequency, intensity, total duration, and cumulative heat (a hot extreme event is defined as at least three consecutive days with daily temperatures exceeding the 90th percentile local threshold during the summer season, see Definitions of Hot Extremes and Related Metrics in Methods for detailed definitions). The simulations are compared against ERA5 reanalysis data (the fifth-generation reanalysis from the European Centre for Medium-Range Weather Forecasts[38]) for the period 1979 to 2019. Both HR-CESM and CMIP6 faithfully reproduce the spatial distribution of hot extreme total duration (our primary measure for hot extreme events, see Definitions of Hot Extremes and Related Metrics in Methods), with only slight differences in magnitude (Supplementary Fig. 1a–d). The same holds true for the occurrence frequency, intensity and cumulative heat distributions as well (Supplementary Fig. 1e–p). In addition, we evaluate the models' ability to represent observed trends in hot extremes over the historical period (Supplementary Fig. 2). While both HR-CESM and CMIP6 capture regions with significant increases in hot extreme duration, they tend to slightly overestimate the trends. Overall, the models show high fidelity in simulating key characteristics of hot extremes. However, we note that increasing the resolution to eddy-resolving scales in HR-CESM provides limited improvement in their climatological simulation compared with CMIP6, a finding consistent with previous research[39].

We next examine the projected changes of hot extremes in HR-CESM under the high emission scenario of Representative Concentration Pathway 8.5 (RCP8.5). By the end of the 21st century (2081–2100), substantial global increases in the total duration, occurrence frequency, intensity, and cumulative heat of hot extremes are projected compared to the historical period (1981–2000, Fig. 1a–d). The global averaged total duration of hot extremes is expected to rise from 2.57 days per summer to 66.46 days per summer, a more than 25-fold increase (Fig. 1e). The increase in duration, together with a higher intensity, drives a substantial rise in cumulative heat, with future levels projected to exceed current values by over 70 times (Fig. 1e). In addition, there is a near linear-relationship between the rise in hot extremes and summer mean temperature increase from 1979 to 2100, along with a hemispheric asymmetry in the response (Fig. 1f). The more pronounced increase in hot extremes in the Northern Hemisphere is attributed to enhanced warming, driven by the greater land coverage in this region. These projected features align with previous findings[40–42], confirming the robustness of hot extreme projections under warming conditions by HR-CESM.

The projected changes in hot extreme events exhibit pronounced spatial heterogeneity (Fig. 1a–d). Regions such as northwestern and eastern coastal North America, the Amazon region in northern South America,

southern Europe, the Middle East, northern and central Africa, and South Asia experience larger increases in total duration (Fig. 1a). In contrast, regions like the central U.S., northeastern Canada, southern South America, northern Eurasia, the Sahel, and Australia show a suppressed rise. The contrast in regional variability aligns closely with changes in intensity and cumulative heat, while the frequency of events shows an opposite trend. The relatively smaller increase in frequency is due to the longer duration of individual heatwave events under strong warming towards the end of the century, which reduces the number of separate occurrences in a given period.

We verify the hot extreme projections using CMIP6, across different warming periods and thresholds. The projected rising trend and hemispheric asymmetry for 2031-2050 are evident in CMIP6, albeit with a lower amplitude (Supplementary Fig. 3). By mid-century, the global averaged hot extreme duration is projected to be approximately 11 times the current value (Supplementary Fig. 3e), representing 40% of the increase expected in HR-CESM by 2100. Importantly, the spatial variability of projected hot extremes in CMIP6 closely mirrors that of HR-CESM (Supplementary Fig. 3a–d), displaying similar hot and cold spot patterns, though the increase is more subdued in southern Europe. We note that CMIP6 projections extend only to mid-century and thus do not capture the substantial lengthening of individual heatwave events expected under stronger late-century warming, resulting in frequency changes that do not exhibit the inverse relationship with duration observed in HR-CESM.

The above projections are based on a fixed threshold referenced to the historical period (T90$_{hist}$). We also validate the results using a varying threshold referenced to future warming periods (T90$_{future}$, see Definitions of Hot Extremes and Related Metrics in Methods). Compared to the fixed threshold, the varying threshold results in an overall shorter but still statistically significant increase in hot extreme total duration (Supplementary Fig. 4a). The spatial distribution of hot extreme increase remains similar, except for a less pronounced response in South Asia (Supplementary Fig. 4a). To ensure consistent identifications of hot and cold spots across HR-CESM, CMIP6, and different thresholds, southern Europe and South Asia are excluded from the hot spot regions in the subsequent analysis when comparing temperature probability density functions (PDFs) between these regions. The exclusion is also supported by the K-means clustering results (see K-means Clustering Analysis in Methods) as discussed later.

Drivers of spatial heterogeneity in future hot extremes

Changes in temperature mean and variability are widely recognized as key factors influencing projections of hot extremes under warming[10,43,44]. However, the spatial distribution of mean temperature changes shows little similarity to that of projected hot extremes changes, with only a weak and insignificant positive correlation under the RCP8.5 scenario in HR-CESM (Supplementary Fig. 5a, b). Similarly, no clear spatial correlation is found between projected hot extremes and temperature variability changes (Fig. 2b, d), indicating that regional disparities in heatwave projections cannot be explained by these two factors. Instead, at 83% of global grid points, projected changes in hot extremes are negatively correlated with historical temperature variability (Fig. 2a). A linear regression between the spatial anomalies of these variables shows a significant negative correlation, with a coefficient of −0.73 above the 99% confidence level (Fig. 2c). This negative correlation also holds across over 71% of the global area when applying a varying threshold (Supplementary Fig. 4). These findings are further validated in CMIP6 (Supplementary Fig. 5c, d, S6), revealing a consistent negative correlation between the increase in hot extremes and baseline temperature variability across 93% of the global. Together, these results suggest the robust role of baseline temperature variability in shaping the future geographical distribution of hot extremes, consistent with previous findings that extreme-event scaling strongly depends on native variability and helps explain the contrasting responses between tropical and mid- to high-latitude regions[21].

To better assess the relative contributions of temperature mean and variability in driving regional differences in hot extreme responses, we
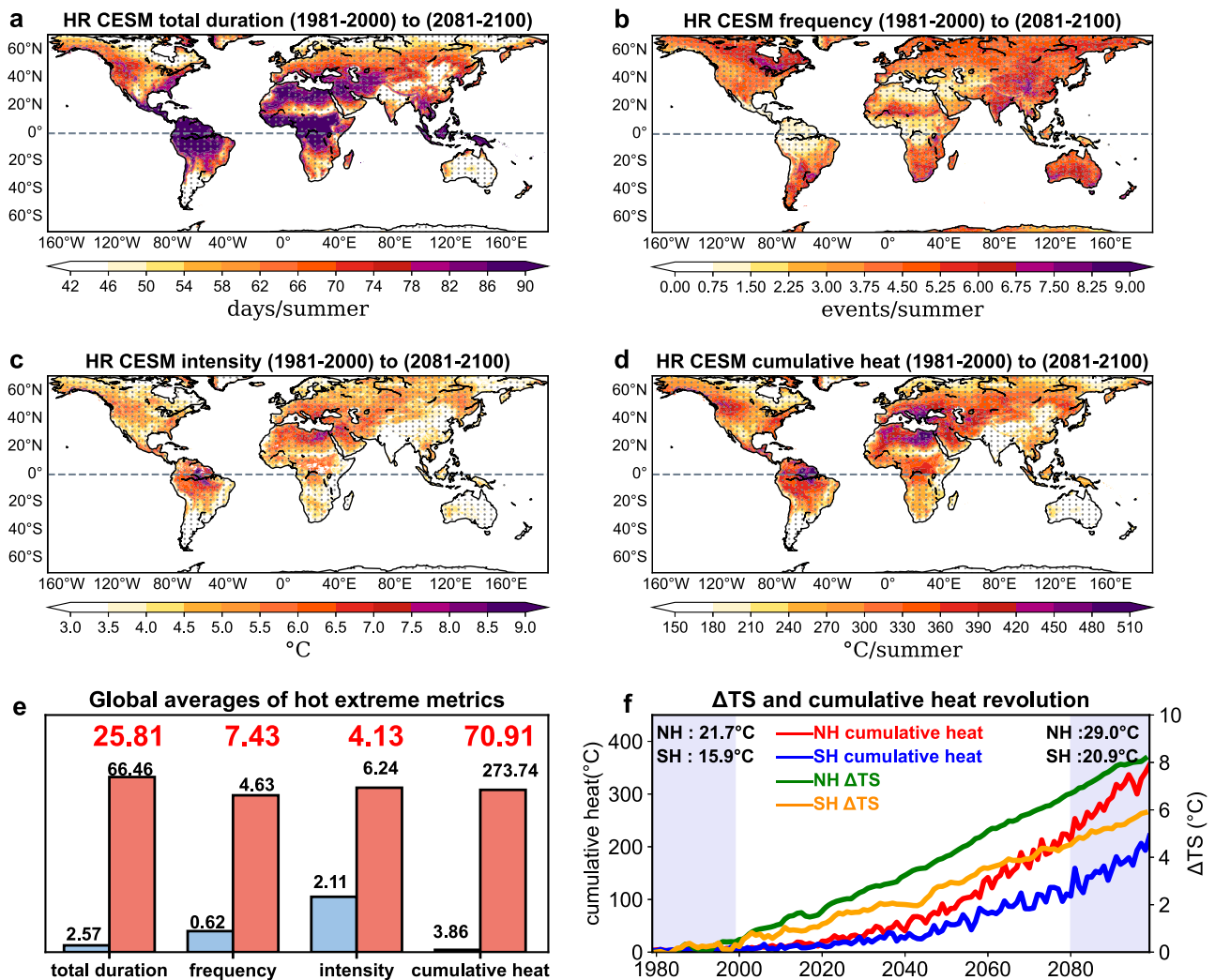
Fig. 1 | Responses of hot extremes to anthropogenic warming in the high-resolution Community Earth System Model (HR-CESM). Differences in summer season (JJA in the Northern Hemisphere and DJF in the Southern Hemisphere) averages of total duration (days per summer, **a**), frequency (events per summer, **b**), intensity (°C, **c**) and cumulative heat (°C per summer, **d**) for hot extreme events between historical (1981-2000) and future simulations (2081-2100) in HR-CESM. Differences above the 95% confidence level based on a two-sided Student's test are shaded by gray dots. **e** Global averages (70°S–70°N, areas without hot extremes are assigned a value of 0) of hot extreme metrics in historical (blue bars) and future simulations (red bars), with corresponding values labeled above the bars. The red numbers at the top indicate the fold increases between future and historical values. **f** Time series of cumulative heat averaged for the Northern Hemisphere (15°N–70°N, red line), Southern Hemisphere (15°S–70°S, blue line), along with summer surface temperature changes relative to 1979–1984 (5-year moving average) for the Northern Hemisphere (JJA, 15°N–70°N, green line) and Southern Hemisphere (DJF, 15°S–70°S, orange line). Shaded regions in (**f**) outline the historical and future periods analyzed, with mean summer temperatures for both hemispheres labeled for the respective periods.

analyzed temperature PDFs for both high- and low-response regions. To minimize uncertainties in region selection, we apply the K-means clustering approach (see K-means Clustering Analysis in Methods), which produces high- and low-response regions that closely match the hot and cold spots consistently identified across HR-CESM, CMIP6, and various threshold definitions (Supplementary Fig. 7a), confirming the robustness of the classification.

The temperature PDFs of these two groups are distinct, with high-response regions exhibiting much narrower distribution and lower historical temperature variability than low-response regions (blue lines in Fig. 2f, g). Specifically, the standard deviation of historical temperatures (the square root of variance) in high-response regions is only one-quarter that of the low-response regions (blue bars in Fig. 2f, g). However, the projected total duration of future hot extremes in high-response regions is approximately twice that of low-response regions (red bars in Fig. 2f, g). Under warming conditions, both temperature PDFs shift rightward, leading to a marked increase in the proportion of hot extreme days (red lines in Fig. 2f, g). Projections show that T90p, representing the proportion of temperatures

exceeding the 90th percentile, will rise to 79.8% in high-response regions in the future, compared to 45.3% in low-response regions. Interestingly, the mean temperature shifts are comparable in both regions, with a slightly greater warming observed in low-response regions (5.6 °C increase in high-response regions and 5.9 °C in low-response regions). This suggests that the greater increase in hot extremes in high-response regions is not attributed to differences in mean temperature shifts.

The impact of baseline temperature variability on the increase in T90p is further quantified using idealized Gaussian temperature distributions (Fig. 2e). For the same 6 °C warming, T90p for temperature profiles with low baseline variability (one standard deviation) is expected to rise to nearly 100%, while for profiles with high baseline variability (four standard deviations), T90p increases to only 41.3%.

The negative correlation between baseline temperature variability and hot extreme intensification can be interpreted within the signal-to-noise ratio framework[22], where mean temperature change represents the signal and temperature variability represents the noise. Regions with higher signal-to-noise ratios are expected to experience more frequent hot extremes,
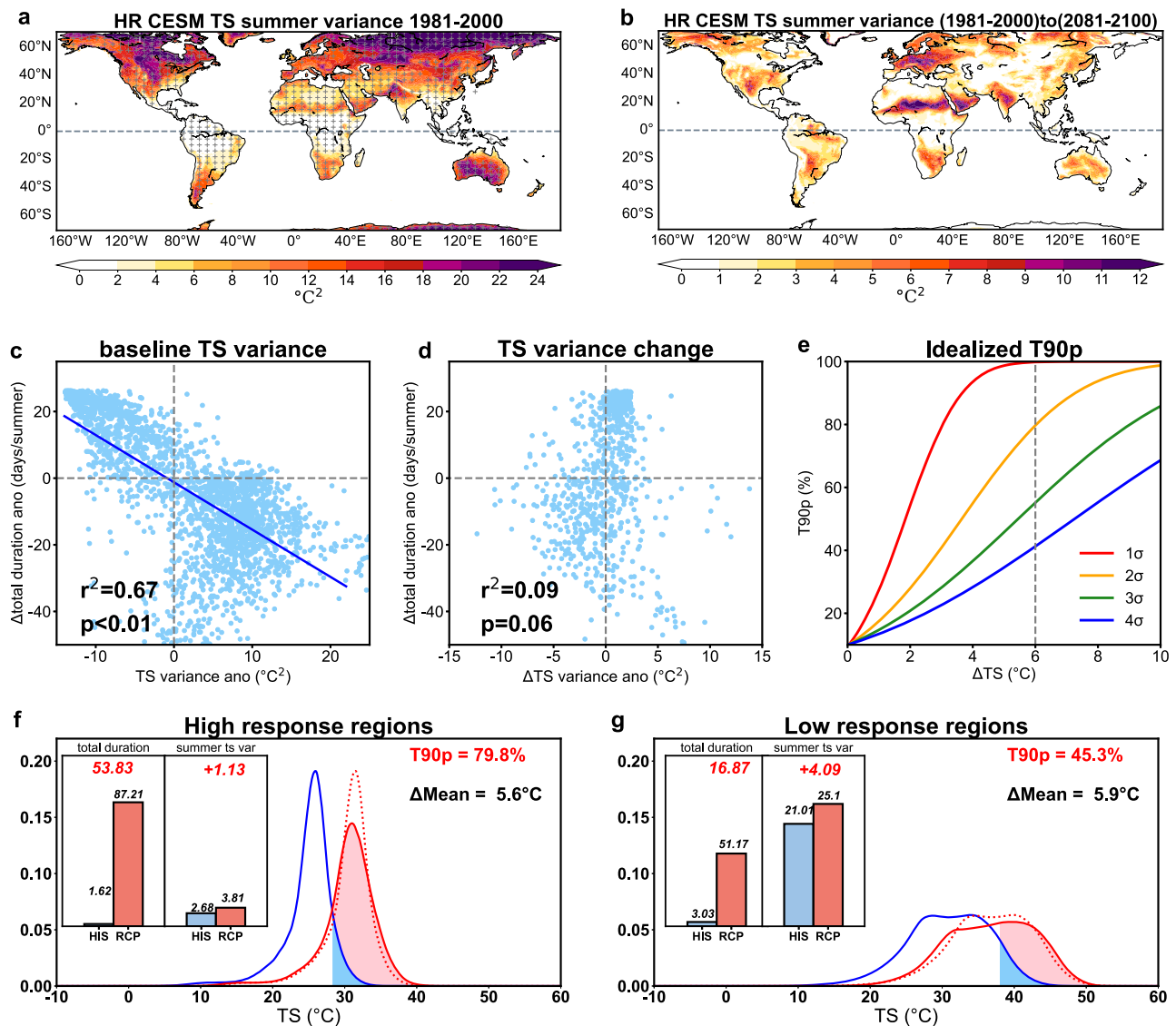
Fig. 2 | Role of temperature variance in driving the spatial heterogeneity of future hot extremes. Summer season averaged temperature variance in historical simulations (1981–2000, **a**) and the difference of that between future (2081-2100) and historical simulations (1981–2000) in the high-resolution Community Earth System Model (HR-CESM) (**b**). Grid points with a negative correlation between hot extreme change and historical temperature variance are shaded by plus markers in (**a**). **c** Scatter plot between anomalous hot extreme total duration changes (future minus historical) and anomalous historical temperature variance (historical) in the regions highlighted by plus markers in (**a**). **d** Scatter plot between anomalous hot extreme total duration changes (future minus historical) and anomalous temperature variance changes (future minus historical) in the regions highlighted by plus markers in (**a**). The anomalous values plotted in (**c**) and (**d**) are computed as the absolute values minus the global mean. **e** Changes in T90p (the proportion of temperatures exceeding the 90th percentile) relative to different standard deviation levels (from 1σ to 4σ) and mean temperature shifts based on idealized Gaussian distributions. **f** Temperature probability distribution functions (PDFs) for high-response regions identified by K-means clustering in historical (blue solid line) and future (red solid line) simulations in HR-CESM. The red dashed line represents the shifted PDF corresponding to the mean temperature change. Bar plots show region-averaged total duration and temperature variance for historical (blue) and future (red) periods, with corresponding values and fold increases labeled above the bars. **g** Same as (**f**) but for low-response regions.

whereas in regions with higher variability (greater noise), a stronger warming signal is required to exceed the noise, leading to a later time of emergence, thereby reducing the occurrence probability of hot extremes.
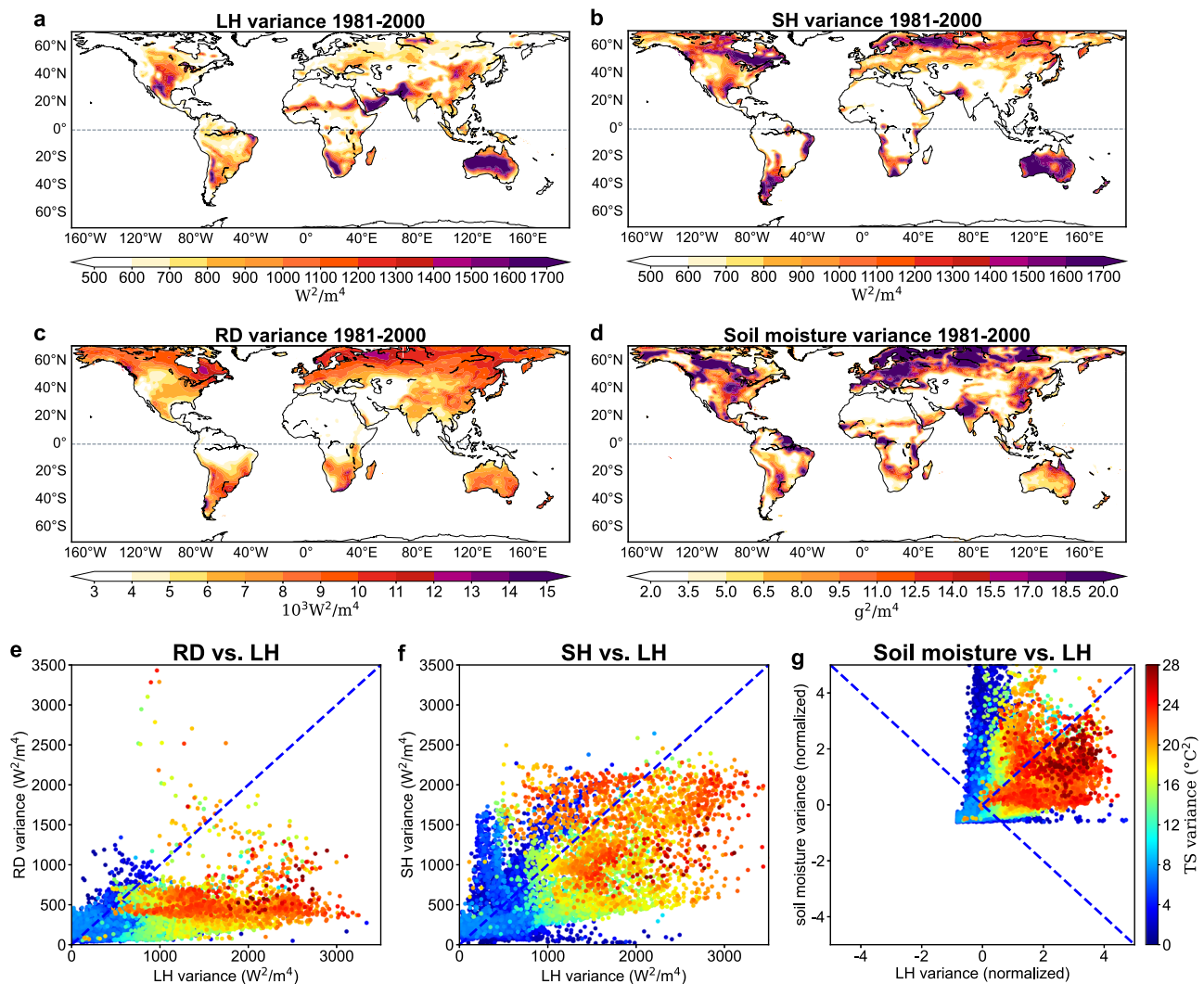
Physical processes influencing baseline temperature variability
To identify the physical processes contributing to the spatial variability of baseline temperature variability, we examine latent heat flux (LH), sensible heat flux (SH), and downwelling radiation (RD), all of which influence the surface energy balance that drives land surface temperature and, consequently, temperature variability[10,43]. Spatial comparison shows that across most of the globe, baseline temperature variance closely aligns with LH variance, except in the northern high latitudes (north of 50 °N), where it tends to be more influenced by SH and RD (Fig. 3a–c). After excluding this

region, scatter plots clearly reveal that the temperature variance is primarily driven by LH variance, with a smaller contribution from SH and a minimal impact from RD (Fig. 3e, f).

Soil moisture has been widely reported to influence the partition between LH and SH through land-atmospheric coupling[24,34,45], emphasizing its potential role in driving temperature variability. This is corroborated by the strong spatial resemblance between temperature and soil moisture variance (Fig. 3d). A closer examination of the scatter plots reveals two distinct regimes (Fig. 3g). In the low-temperature variance regime, the scatter cloud is nearly vertical, indicating the predominant role of soil moisture. In the high-temperature variance regime, the scatter cloud aligns at a 45° angle, suggesting joint impacts from soil moisture and LH. The difference is likely linked to local dry or wet conditions,

Fig. 3 | Physical processes contributing to the spatial heterogeneity of baseline temperature variability. Summer season averaged variance of latent heat flux (W^2 m^{-4}, **a**), sensible heat flux (W^2 m^{-4}, **b**), downwelling radiation (W^2 m^{-4}, **c**), and soil moisture (g^2 m^{-4}, **d**) in historical simulations (1981–2000) in the high-resolution Community Earth System Model (HR-CESM). **e** Scatter plot of historical temperature variance in high- and low-response regions identified by K-means clustering (colored dots) as a function of both latent heat flux variance (horizontal axis) and downwelling radiation variance (vertical axis). **f**, **g** Same as (**e**) but with sensible heat flux and soil moisture variance on the vertical axis. Note that latent heat flux and soil moisture variance in (**g**) are normalized to eliminate scale differences between the two variables.

which affect the sensitivity of evapotranspiration responses to soil moisture, as suggested by previous studies[34,45]. These findings, consistent with prior research, support the critical role of soil moisture in modulating temperature variability.

We also examine the role of atmospheric dynamics in affecting temperature variability. In mid- and high-latitude regions, synoptic-scale storms are often assumed to dominate variability. However, timescale decomposition reveals only a minor contribution from synoptic scales, with intraseasonal (10–30 days) fluctuations accounting for the bulk of total variability (Supplementary Fig. 8a, b). Furthermore, stationary wave analysis shows that, in the Northern Hemisphere—particularly over northwestern and eastern coastal North America and the Mediterranean—high-response (low temperature variability) regions are closely linked to persistent highs (Supplementary Fig. 8c). In contrast, this dynamic is less relevant in the Southern Hemisphere, consistent with previous studies showing that temperature extremes there are more strongly influenced by non-local forcing, where heat is advected from neighboring regions[44,46,47]. Overall, these results indicate that the contribution of atmospheric circulations to temperature variability is more localized, with stationary waves playing only a limited global role.

Century-scale persistence in land-atmosphere coupling

The role of baseline temperature variability in driving the spatial distribution of future hot extremes over the next century raises an important question: what is the key driver behind this century memory? The above analysis reveals a strong link between soil moisture and temperature variability, primarily operating through a negative soil moisture-evaporation-temperature feedback according to previous studies[34]. This feedback is often referred to as land-atmosphere coupling and can be effectively captured by the correlation between the detrended evaporation and surface temperature[48]. Regions characterized by both low hot extreme response and high baseline temperature variability coincide with areas of active land-atmosphere coupling (Fig. 4a). Notably, the coupling remains remarkably stable across historical and future simulations (Fig. 4a, b), with nearly 95% of global areas showing persistent patterns (Fig. 4c). The spatial match of active and inactive land-atmosphere coupling areas between past and future simulations shows a high correlation of 0.86 (Fig. 4d), underscoring the persistence of this distribution over a century timescale. This enduring pattern is also corroborated by multiple CMIP6 models, indicating that it is not model-specific (Fig. 4e). The results suggest that the spatial distribution of baseline temperature variability is intrinsically tied to land-atmosphere
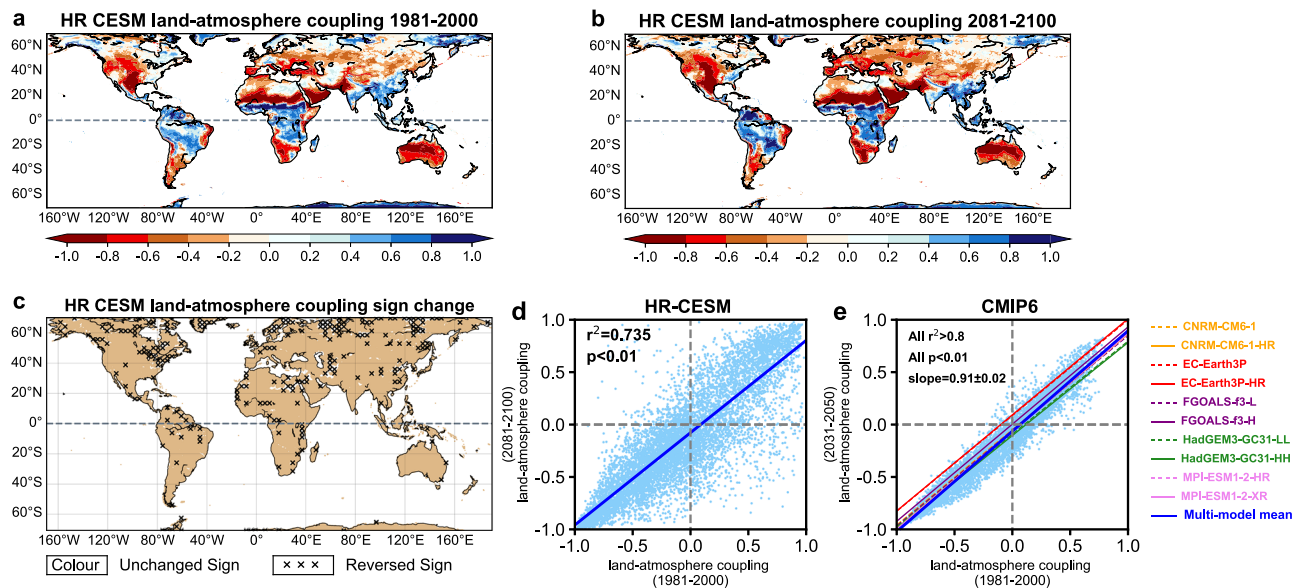
Fig. 4 | Persistence in the spatial distribution of land-atmosphere coupling. Summer season averaged land-atmosphere coupling, defined as the correlation between detrended surface temperature and evaporation, in historical (1981–2000, **a**) and future simulations (2081-2100, **b**) in the high-resolution Community Earth System Model (HR-CESM), where negative (positive) correlations represent active (inactive) coupling. **c** Coupling sign changes between future and historical simulations, with unchanged signs in color and reversed signs marked by 'x'. **d** Scatter plot between historical and future land-atmosphere coupling in HR-CESM, with 94.8% of global areas showing persistent signs and a correlation coefficient of 0.86 above the 99% confidence level. **e** Scatter plot for Coupled Model Intercomparison Project Phase 6 (CMIP6) simulations, with 99.3% of global areas showing persistent signs and a coefficient of 0.97 above the 99% confidence level.

coupling, which operates over a long time and anchors the spatial heterogeneity of future hot extremes.

Discussion

Using eddy-resolving HR-CESM simulations and multiple model results from CMIP6, we identify baseline temperature variability as a key factor shaping the uneven distribution of future hot extremes, a relationship interpretable within the signal-to-noise ratio framework. The results are validated across various climate models, warming levels, and thresholds. The baseline temperature variability is anchored by persistent land-atmosphere coupling, which operates over century timescales and sustains the spatial heterogeneity of future hot extremes. Moreover, the coupling primarily influences the distribution of temperature variability through soil moisture and latent heat flux, consistent with the current understanding of soil moisture-temperature feedback dynamics, and further supporting the robustness of the results, with atmospheric dynamics playing only a limited role.

Existing studies have emphasized the role of changes in temperature mean and variability in determining hot extreme projections under warming[10,18,43,44,49,50], underscoring the need for accurate representations of these factors for both historical and future periods to ensure reliable estimates of future hot extremes. However, the task remains challenging due to substantial uncertainties in projected changes in temperature mean and variability in future periods. Our findings show that regional variations in projected hot extremes are only weakly connected to changes in temperature mean or variability under warming. Instead, baseline temperature variability primarily determines the global pattern of hot extreme projections, highlighting it as a potential predictor for assessing regional variations in future hot extreme responses. These findings provide a simplified framework for assessing the geographic distribution of future hot extremes based on historical state without integrating into the future, offering valuable insights for developing more targeted adaptation strategies for regions most vulnerable to extreme heat under climate change. However, the results also stress the importance of more precise and comprehensive observations to quantify historical temperature variability, as well as improved climate models' capability of accurately simulating this variability, to enhance projections of

regional variations in future hot extremes. The findings may be subject to uncertainties due to their reliance on the century-scale persistence of land-atmosphere coupling, which is potentially maintained by soil moisture memory and vegetation dynamics[51–55]. However, the interactions among soil moisture, vegetation, and atmospheric processes at these timescales remain incompletely understood and accurately representing and projecting the coupling remains a major challenge for current climate models[35,56,57].

Methods
High-resolution CESM and CMIP6 simulations
The eddy-resolving high-resolution Community Earth System Model (HR-CESM) simulations with ~0.25° atmosphere and ~0.1° ocean components developed by the National Center for Atmospheric Research (NCAR) are analyzed[58]. The simulations consist of a 500-year preindustrial control run and a 250-year simulation covering historical (1850–2005) and future (2006–2100) climates. Historical forcing is applied from 1850 to 2005, followed by the RCP8.5 scenario (a high greenhouse gas concentration pathway) forcing from 2006 onwards. Daily outputs are used to assess hot extreme events and related variables, comparing two periods: a historical period from 1981 to 2000, and a future period from 2081 to 2100.

Ten climate model simulations from the Coupled Model Intercomparison Project Phase 6 (CMIP6) are examined, including five from the High-Resolution Model Intercomparison Project (HighResMIP[59]) and five pairing low-resolution simulations. The oceanic resolution of these models ranges from 0.1° to 1°, while atmospheric resolution ranges from 0.25° to 1°. The selected models and their specific resolutions are detailed in Supplementary Table 1. Each model includes a 100-year historical and future (under RCP8.5 scenario) simulation from 1950–2050. These models are chosen because they provide both high- and low-resolution versions along with long-term RCP8.5 projections. Hot extreme events during the period overlapping with ERA5 and HR-CESM are analyzed and compared.

Definition of Hot Extremes and Related Metrics
Following previous studies[14,60], a hot extreme event is defined as at least three consecutive days with daily temperatures exceeding the 90th

percentile threshold during summer (JJA in the Northern Hemisphere and DJF in the Southern Hemisphere). The 90th percentile is calculated for each calendar day at each grid point using a 15-day moving window centered around the targeted day over the reference periods[60]. Two thresholds are computed: one reference to the historical period (1979–2019, T90$_{hist}$) and another to future warming periods (2060–2100, T90$_{future}$). Correspondingly, hot extreme projections under anthropogenic warming are evaluated in two ways. For the fixed threshold, hot extremes in both historical and future periods are identified using T90$_{hist}$. For the varying threshold, hot extremes are identified using T90$_{hist}$ for the historical and T90$_{future}$ for the future period. Projected changes in hot extremes using the fixed threshold account for the contribution from mean temperature increases between the historical and future periods, while the varying threshold excludes this effect.

The occurrence frequency is defined as the number of hot extreme events per summer. The intensity of each event is measured by the maximum temperature anomaly above the 90th percentile threshold during the event and then averaged over the summer season. Total duration refers to the cumulative number of days during which hot extreme events occur per summer. Cumulative heat is the sum of temperature anomalies exceeding the 90th percentile threshold across all hot extreme events[14]. Notably, total duration is an effective indicator of projected hot extreme changes, capturing both occurrence frequency and mean duration response (Fig. 1a). It is also the dominant contributor to cumulative heat increase (Fig. 1d), a finding consistent with prior research[14]. Therefore, we use total duration as the primary measure of hot extreme responses in our analyses. Additionally, baseline temperature variability is computed as the variance of daily surface air temperature anomalies, after removing the linear trend, over the historical reference period (1981–2000).

K-means clustering analysis

K-means clustering is applied to identify regions with high or low hot extreme responses based on projected changes in total duration and historical temperature variance[61]. Both variables are normalized (ranging from −2.5 to 2.5 standard deviation) and divided into five categories, labeled from −2 to 2, with each category spanning one standard deviation. This ensures comparability between the variables and prevents one from dominating the clustering due to scale differences. The K-means algorithm is then applied to the processed data and repeated 1000 times with random initial cluster centroids, yielding an optimized clustering of 5. The two clusters with the largest and opposite variations in hot extreme changes and temperature variance are selected, which gives the high- and low-response regions shown in Supplementary Fig. 7. As illustrated in the spatial map of hot extreme change and temperature variance (Fig. 1a and Fig. 2a), high-response regions correspond to areas with low historical temperature variance, and vice versa. These regions also closely match the hot and cold spots consistently identified across HR-CESM, CMIP6, and different threshold definitions, confirming the robustness of the classification. Note that in all identified regions, historical temperature variance is markedly lower in high-response regions compared to low-response regions. However, due to differing geographical locations, the temperature PDFs in these regions exhibit distinct mean temperatures, which can obscure the overall PDF shape when combined. To enhance clarity, the temperature PDFs for North Africa and Northern Eurasia (regions with distinct mean temperatures) are plotted separately (Supplementary Fig. 7b, c), while the remaining regions are shown in Fig. 2f, g.

Data availability

ERA5 reanalysis can be downloaded from https://doi.org/10.24381/cds.bd0915c6. The CESM simulations can be achieved through https://ihesp.github.io/archive/products/ds_archive/Sunway_Runs.html. The CMIP6 data can be downloaded from https://pcmdi.llnl.gov/CMIP6/. Data used to produce the figures in the main text and the supplementary information can be found at https://github.com/ChelseaTang1017/Land-Hot-Extremes/.

Code availability

Python and Matlab codes to reproduce the analyses are available upon request from the corresponding author.

References

1. Lobell, D. B. & Field, C. B. Global scale climate–crop yield relationships and the impacts of recent warming. *Environ. Res. Lett.* **2**, 014002 (2007).
2. Campbell, S., Remenyi, T. A., White, C. J. & Johnston, F. H. Heatwave and health impact research: a global review. *Health Place* **53**, 210–218 (2018).
3. Domeisen, D. I. V. et al. Prediction and projection of heatwaves. *Nat. Rev. Earth Environ.* **4**, 36–50 (2022).
4. Yin, J. et al. Future socio-ecosystem productivity threatened by compound drought–heatwave events. *Nat. Sustain* **6**, 259–272 (2023).
5. Robine, J.-M. et al. Death toll exceeded 70,000 in Europe during the summer of 2003. *Comptes Rendus Biologies* **331**, 171–178 (2008).
6. García-León, D. et al. Current and projected regional economic impacts of heatwaves in Europe. *Nat. Commun.* **12**, 5807 (2021).
7. WMO. *Atlas of Mortality and Economic Losses from Weather, Climate and Water Extremes* Vol. 1123 (WMO, 2014).
8. Seneviratne, S. I. et al. Weather and Climate Extreme Events in a Changing Climate. *Climate Change 2021: The Physical Science Basis. Contribution of Working Group I to the Sixth Assessment Report of the Intergovernmental Panel on Climate Change* 1513–1766 https://doi.org/10.1017/9781009157896.013 (2021).
9. Seneviratne, S. I., Donat, M. G., Pitman, A. J., Knutti, R. & Wilby, R. L. Allowable CO2 emissions based on regional and impact-related climate targets. *Nature* **529**, 477–483 (2016).
10. Vogel, M. M. et al. Regional amplification of projected changes in extreme temperatures strongly controlled by soil moisture-temperature feedbacks. *Geophys. Res. Lett.* **44**, 1511–1519 (2017).
11. Turnau, R., Robinson, W. A., Lackmann, G. M. & Michaelis, A. C. Model projections of increased severity of heat waves in Eastern Europe. *Geophys. Res. Lett.* **49** (2022).
12. Perkins, S. E. & Alexander, L. V. On the Measurement of Heat Waves. *J. Clim.* **26**, 4500–4517 (2013).
13. Russo, S. et al. Magnitude of extreme heat waves in present climate and their projection in a warming world. *JGR Atmos.* **119** (2014).
14. Perkins-Kirkpatrick, S. E. & Lewis, S. C. Increasing trends in regional heatwaves. *Nat. Commun.* **11**, 3357 (2020).
15. Teng, H., Leung, R., Branstator, G., Lu, J. & Ding, Q. Warming pattern over the Northern Hemisphere Midlatitudes in Boreal Summer 1979–2020. *J. Climate* **35** (2022).
16. Gao, Y. More frequent and persistent heatwaves due to increased temperature skewness projected by a high-resolution earth system model. *Geophys. Res. Lett.* **50**, e2023GL105840.
17. Loikith, P. C. & Neelin, J. D. Non-Gaussian cold-side temperature distribution tails and associated synoptic meteorology. *J. Clim.* **32**, 8399–8414 (2019).
18. Lavell, A. et al. in *Managing the Risks of Extreme Events and Disasters to Advance Climate Change Adaptation. A Special Report of Working Groups I and II of the Intergovernmental Panel on Climate Change (IPCC)* (eds Field, C. B. et al.)(Cambridge University Press, 2012).
19. Harrington, L. J. et al. Poorest countries experience earlier anthropogenic emergence of daily temperature extremes. *Environ. Res. Lett.* **11**, 055007 (2016).
20. Borodina, A., Fischer, E. M. & Knutti, R. Potential to constrain projections of hot temperature extremes. *J. Clim.* **30**, 9949–9964 (2017).
21. Simolo, C. & Corti, S. Quantifying the role of variability in future intensification of heat extremes. *Nat. Commun.* **13**, 7930 (2022).

22. Padalino, C., Lickley, M. & Solomon, S. Heat wave time of emergence patterns: a matter of definition. *Environ. Res. Commun.* **6**, 051005 (2024).

23. Vogel, M. M., Zscheischler, J., Fischer, E. M. & Seneviratne, S. I. Development of future heatwaves for different hazard thresholds. *JGR Atmos.* **125**, e2019JD032070 (2020).

24. Seneviratne, S. I. et al. Impact of soil moisture-climate feedbacks on CMIP5 projections: First results from the GLACE-CMIP5 experiment. *Geophys. Res. Lett.* **40**, 5212–5217 (2013).

25. Douville, H., Colin, J., Krug, E., Cattiaux, J. & Thao, S. Midlatitude daily summer temperatures reshaped by soil moisture under climate change. *Geophys. Res. Lett.* **43**, 812–818 (2016).

26. Diro, G. T., Sushama, L. & Huziy, O. Snow-atmosphere coupling and its impact on temperature variability and extremes over North America. *Clim. Dyn.* **50**, 2993–3007 (2018).

27. Coumou, D., Lehmann, J. & Beckmann, J. The weakening summer circulation in the Northern Hemisphere mid-latitudes. *Science* **348**, 324–327 (2015).

28. Horton, D. E. et al. Contribution of changes in atmospheric circulation patterns to extreme temperature trends. *Nature* **522**, 465–469 (2015).

29. Rousi, E., Kornhuber, K., Beobide-Arsuaga, G., Luo, F. & Coumou, D. Accelerated western European heatwave trends linked to more-persistent double jets over Eurasia. *Nat. Commun.* **13**, 3851 (2022).

30. Arblaster, J. M. & Alexander, L. V. The impact of the El Niño-Southern Oscillation on maximum temperature extremes. *Geophys. Res. Lett.* **39**, 2012GL053409.

31. Miralles, D. G., Teuling, A. J., van Heerwaarden, C. C. & Vilà-Guerau de Arellano, J. Mega-heatwave temperatures due to combined soil desiccation and atmospheric heat accumulation. *Nat. Geosci.* **7**, 345–349 (2014).

32. Luo, M. & Lau, N.-C. Summer heat extremes in northern continents linked to developing ENSO events. *Environ. Res. Lett.* **15**, 074042 (2020).

33. Koster, R. D., Chang, Y., Wang, H. & Schubert, S. D. Impacts of local soil moisture anomalies on the atmospheric circulation and on remote surface meteorological fields during boreal summer: a comprehensive analysis over North America. *J. Climate* **29** (2016).

34. Seneviratne, S. I. et al. Investigating soil moisture–climate interactions in a changing climate: a review. *Earth-Sci. Rev.* **99**, 125–161 (2010).

35. Cheng, S., Huang, J., Ji, F. & Lin, L. Uncertainties of soil moisture in historical simulations and future projections. *JGR Atmos.* **122**, 2239–2253 (2017).

36. Qu, X. & Hall, A. On the persistent spread in snow-albedo feedback. *Clim. Dyn.* **42**, 69–81 (2014).

37. Shepherd, T. G. Atmospheric circulation as a source of uncertainty in climate change projections. *Nat. Geosci.* **7**, 703–708 (2014).

38. Hersbach, H. et al. The ERA5 global reanalysis. *Quart. J. R. Meteor. Soc.* **146**, 1999–2049 (2020).

39. Schiemann, R. et al. The resolution sensitivity of Northern Hemisphere blocking in four 25-km atmospheric global circulation models. *J. Clim.* **30**, 337–358 (2017).

40. Almazroui, M. et al. Projected changes in climate extremes using CMIP6 simulations over SREX regions. *Earth Syst. Environ.* **5**, 481–497 (2021).

41. Stouffer, R. J., Manabe, S. & Bryan, K. Interhemispheric asymmetry in climate response to a gradual increase of atmospheric CO2. *Nature* **342**, 660–662 (1989).

42. Vogel, M. M., Hauser, M. & Seneviratne, S. I. Projected changes in hot, dry and wet extreme events' clusters in CMIP6 multi-model ensemble. *Environ. Res. Lett.* **15**, 094021 (2020).

43. Bathiany, S., Dakos, V., Scheffer, M. & Lenton, T. M. Climate models predict increasing temperature variability in poor countries. *Sci. Adv.* **4**, eaar5809 (2018).

44. Perkins, S. E. A review on the scientific understanding of heatwaves—their measurement, driving mechanisms, and changes at the global scale. *Atmos. Res.* **164–165**, 242–267 (2015).

45. Berg, A. et al. Impact of soil moisture–atmosphere interactions on surface temperature distribution. *J. Clim.* **27**, 7976–7993 (2014).

46. Marshall, A. G. et al. Intra-seasonal drivers of extreme heat over Australia in observations and POAMA-2. *Clim. Dyn.* **43**, 1915–1937 (2014).

47. Pezza, A. B., Van Rensch, P. & Cai, W. Severe heat waves in Southern Australia: synoptic climatology and large scale connections. *Clim. Dyn.* **38**, 209–224 (2012).

48. Seneviratne, S. I., Lüthi, D., Litschi, M. & Schär, C. Land–atmosphere coupling and climate change in Europe. *Nature* **443**, 205–209 (2006).

49. Ruff, T. W. & Neelin, J. D. Long tails in regional surface temperature probability distributions with implications for extremes under global warming. *Geophys. Res. Lett.* **39**, 2011GL050610 (2012).

50. Schär, C. et al. The role of increasing temperature variability in European summer heatwaves. *Nature* **427**, 332–336 (2004).

51. Koster, R. D. et al. GLACE: The Global Land–Atmosphere Coupling Experiment. Part I: Overview. *J. Hydrometeorol.* **7**, 590–610 (2006).

52. Combe, M., De Arellano, J. V.-G., Ouwersloot, H. G. & Peters, W. Plant water-stress parameterization determines the strength of land–atmosphere coupling. *Agric. For. Meteorol.* **217**, 61–73 (2016).

53. Zhu, Q. et al. Present and future changes in land-atmosphere coupling of water and energy over extratropical forest regions. *J. Geophys. Res.* **128**, e2022JD037887.

54. Esit, M. et al. Seasonal to multi-year soil moisture drought forecasting. *npj Clim. Atmos. Sci.* **4**, 16 (2021).

55. Svenning, J. & Sandel, B. Disequilibrium vegetation dynamics under future climate change. *Am. J. Bot.* **100**, 1266–1286 (2013).

56. Donat, M. G., Pitman, A. J. & Seneviratne, S. I. Regional warming of hot extremes accelerated by surface energy fluxes. *Geophys. Res. Lett.* **44**, 7011–7019 (2017).

57. Mueller, B. & Seneviratne, S. I. Systematic land climate and evapotranspiration biases in CMIP5 simulations. *Geophys. Res. Lett.* **41**, 128–134 (2014).

58. Chang, P. et al. An unprecedented set of high-resolution earth system simulations for understanding multiscale interactions in climate variability and change. *J. Adv. Model Earth Syst.* **12** (2020).

59. Haarsma, R. J. et al. High Resolution Model Intercomparison Project (HighResMIP v1.0) for CMIP6. *Geosci. Model Dev.* **9**, 4185–4208 (2016).

60. Fischer, E. M. & Schär, C. Future changes in daily summer temperature variability: driving processes and role for temperature extremes. *Clim. Dyn.* **33**, 917–935 (2009).

61. Chattopadhyay, A., Nabizadeh, E. & Hassanzadeh, P. Analog forecasting of extreme-causing weather patterns using deep learning. *J. Adv. Model Earth Syst.* **12** (2020).

Author contributions

Z.T. performed most of the analyses under X.M.'s instruction. S.Z. detected the hot extremes and assisted with data processing. X.M. conceived the central idea, designed the study and wrote the manuscript. L.W. supervised the project. W.C. contributed to discussions on physical mechanisms influencing temperature variability. Z.J., Z.C., and B.G. contributed to interpreting the results and improving the manuscript.

Competing interests

The authors declare no competing interests.

Additional information

Publisher's note Springer Nature remains neutral with regard to jurisdictional claims in published maps and institutional affiliations.